Macromolecular organization of the pyoverdine biosynthetic pathway in *Pseudomonas aeruginosa*.

Véronique Gasser[1,2], Morgane Malrieu[3], Anne Forster[1,2], Yves Mély[3], Isabelle J Schalk[1,2], and Julien Godet[3,4,✉]

[1]Université de Strasbourg, UMR7242, ESBS, Bld Sébastien Brant, F-67413 Illkirch, Strasbourg, France
[2]CNRS, UMR7242, ESBS, Bld Sébastien Brant, F-67413 Illkirch, Strasbourg, France
[3]Laboratoire de BioImagerie et Pathologies, UMR CNRS 7021, Université de Strasbourg, Illkirch, France
[4]Groupe Méthode Recherche Clinique, Hôpitaux Universitaires de Strasbourg, France

The biosynthesis of the pyoverdine siderophore in *Pseudomonas aeruginosa* inlvolves multiple enzymes including Non-Ribosomal Peptide Synthetases (NRPS). We used *in vitro* single-molecule tracking and FRET–FLIM (Förster resonance energy transfer measured by fluorescence lifetime microscopy) to explore the spatial partitioning of the ornithine hydroxylase PvdA and to characterize its interactions with NRPS. The statistical description of thousands of single PvdA traces in cells using jump distance distribution analysis showed PvdA was mostly diffusing bound to large complex in the cytoplasm with a small exchangeable trapped fraction diffusing slower. FRET-FLIM clearly showed PvdA are physically interacting with the four NRPS PvdJ, PvdI, PvdL and PvdD of the pyoverdine pathway in the cellular context. Our data provide evidence for strongly organized multi-enzymatic biosynthetic complexes named siderosomes responsible for the siderophore biosynthesis. PvdA binding mode is strikingly different according to the NRPS it is interacting with suggesting PvdA binding site have co-evolved with the enzymatic active sites of NRPS.

NRPS | pyoverdine | FLIM | single-molecule tracking
Correspondence: ***julien.godet@unistra.fr***

Introduction

To improve fitness, bacteria and fungi have evolved sophisticated machineries to produce secondary metabolites with remarkable structural and functional diversities. Secondary metabolites are often produced by specific and dedicated biosynthetic pathways turning on in response to environmental stimuli. If much is understood about the enzymatic cascades and mechanisms that underlie these biosynthesis, comparatively little is known about their cellular organization (1). There is long-standing hypothesis that enzymes involved in a metabolic pathway must organize into macromolecular complex (2), such that secondary metabolite synthesis is orchestrated by the assembly of sequential enzymes. This process is expected to be widespread (3) (including in eukaryote cells (4)) and with implications for overall biosynthesis efficiency or regulation (4, 5). However observations on such specific multiproteic organisations for secondary metabolite biosynthesis pathways are sparse in the cellular context – and most of them are collected from co-localization observations (2).
Here we used the pyoverdine (PVD) metabolic pathway of *Pseudomonas aeruginosa* as a model system. Pyoverdines (PVD) are large fluorescent siderophores composed by an invariant (1S)-5-amino-2,3-dihydro- 8,9-dihydroxy-1H-pyrimido[1,2-a]quinoline core grafted by the addition of a 6- to 12-amino acids chain (6, 7). In PAO1, PVD synthesis relies on four non-ribosomal peptide synthases (NRPS)(8), PvdL, PvdI, PvdJ and PvdD (8–12) (Figure 1), that direct the synthesis of a PVD precursor peptide of 11 amino acids with the sequence L-Glu–L-Tyr–D-Dab–L-Ser–L-Arg–L-Ser–L-fOHOrn–L-Lys–L-fOHOrn–L-Thr–L-Thr and with the second and third amino acids of the peptide (L-Tyr and D-Dab -D-amino butyric acid-) forming the chromophore. NRPS are fascinating large modular enzymes synthetizing peptides independently from ribosomes (13, 14). Each NRPS module is responsible for the incorporation of a defined monomer into the final product (13) (Figure 1 C). The number of modules and their domain organization controls the structures of the peptide and usually corresponds to the sequence of amino acids in the peptide. The use of non-proteinogenic amino acids, including D-isomers or modified-amino-acids, fatty acids, carboxy acids or carbohydrates as building block is the trademark of NRPS. It explains the sequences diversity of non-ribosomal peptides and derived products (15). While NRPS enzymes generate peptide assembly, accessory and tailoring enzymes responsible for modified amino-acids synthesis are usually associated to NRPSs. These enzymes provide the chemical diversity that makes each secondary metabolite produced by NRPS unique. NRPSs coding genes are found within discrete localized sections of microbial genomes in large bio-synthetic gene clusters (BGCs) (16, 17). Interestingly, many genes coding for enzymes producing non-proteinogenic amino-acids are also found in BGCs and are physically clustered with NRPSs genes. In the PVD pathway, pvdA (18), pvdF(19) and pvdH(12, 20) genes are found in the proximity of NRPS genes in PAO1 genome (Figure 1 B). These enzymes are thus likely co-expressed when the biosynthetic pathway is activated. PvdA, an enzyme involved in PVD bio-synthesis, catalyses the FAD-dependent hydroxylation of the amine side chain of ornithine using NADPH as the electron donor and molecular oxygen to synthesis N5-hydroxy-ornithine (21, 22) (an amino acid present in PVD peptide backbone). Recent findings showed high cellular organization of PVD-related proteins with clusters of PvdA co-

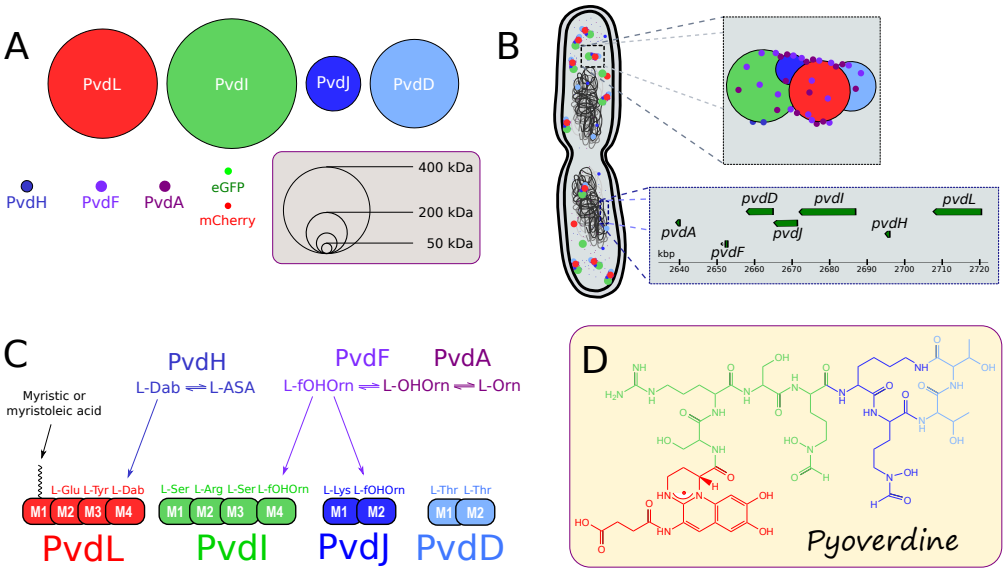

Fig. 1.
(A) Enzymes involved in the cytoplasmic biosynthesis of the pyoverdine precursor. Four large NRPS (PvdL, PvdI, PvdJ and PvdD) are responsible for the synthesis of a 11-AA peptide, incorporating modified AA, produced by PvdH(L-Dab) and by PvdA and PvdF (L-fOH Orn) accessory proteins. Enzyme diameters are proportional to their molecular weight (MW). eGFP and mCherry are presented for MW comparison.
(B) Schematic view of the chromosomic genes and cytoplasmic proteins involved in the early steps of the pyoverdine biosynthetic pathway in Pseudomonas aeruginosa PAO1. Genes coding for NRPSs and accessory proteins are found in a large biosynthetic gene cluster (BGC). Once the pyoverdine pathway is activated, proteins encoded by genes in the BGC are expressed and may organize in siderophore-specific multi-enzymatic biosynthetic complex called siderosomes.
(C) Pyoverdine precursor sequence. During biosynthesis, each NRPSs module is responsible for the incorporation of a defined AA. PVdL (red), PvdI (green), PvdJ (blue) and PvdD (light blue) are acting sequentially to add 3,4,2 and 2 AA, respectively.
(D) Pyoverdine (type I) - the major siderophore synthetized by PAO1 - is a maturated form of the cytoplasmic precursor.

localizing with PvdD, PvdL and PvdJ by fluorescence microscopy (23, 24). Pull-down assay using a recombinant 6His-PvdA protein as a bait captured low amount of PvdI, PvdL, PvdJ and PvdD proteins (24). PvdA has also been shown to interact with PvdJ M2 isolated module in yeast double-hybrid (24). Taken together, these data suggest PvdA would interact with NRPS and could be part of siderophore-specific larger multi-enzymatic complexes named siderosomes (23–25). But clear biochemical characterizations of these complexes are missing – possibly due to extremely dynamic interactions occurring between proteins within siderosomes and/or due to transient formation (25) - and the characterization of such complex in the cellular environment has been barely described. This holds particularly true regarding the interactions of NRPSs with accessory proteins co-expressed in their BGCs. In this context, *in vivo* characterizations with high temporal and/or spatial resolution are required to capture siderosomes organization.

We investigated at the single protein level the localization and dynamics of PvdA in cells using single-particle tracking combined with single-molecule localization using photoactivated localization microscopy (sptPALM (26)). The statistical description of thousands of single PvdA traces in cells evidenced PvdA was mostly diffusing as large complexes in the cytoplasm, at the exception of a small exchangeable restricted fraction diffusing with even lower diffusion rate. We additionally used fluorescence lifetime imaging (FLIM (27)) to evidence interactions between PvdA and the NRPS PvdJ, PvdI, PvdL and PvdD. Although the exact determination of the complex stoichiometry was not accessible from FLIM FRET measurements, our data are consistent with transient interaction of several PvdA on PvdI and PvdL whereas PvdJ most probably harbour one single binding site for PvdA. Our data provide evidence toward complex organization of siderosomes and suggest PvdA binding sites have co-evolved with NRPS module specificity.

Results

PvdA diffuses as large complex in the cytoplasm.

To localize PvdA enzyme in its intracellular environment, we produced strains expressing eGFP, eYFP or PAmCherry fused at PvdA C-terminus as previously described (23, 25). These strains genetically expressed fluorescent PvdA at physiological levels and were able to produce and uptake PVD. Classical epifluorescence microscopy showed PvdA-eGFP was expressed in cells cultured in iron-depleted media. PvdA-eGFP was localized in the cytoplasm. The level of expression of PvdA-eGFP was heterogeneous from cells to cells. No spatial organization was observed along the cell cycle, at the exception of unilateral polar spots in some cells (Figure 2 A-B). However, the resolution of epifluorescence microscopy is too low to totally rule out sub-diffraction limit (250 nm) organizations. To explore more in details the localization and diffusion of single PvdA in live cells, we used Photoactivated Localization Microscopy (PALM) (28) - a single molecule localization microscopy method allowing to determine the position of individual fluorescent molecules with nanometre accuracy in live cells. In PALM, tiny frac-

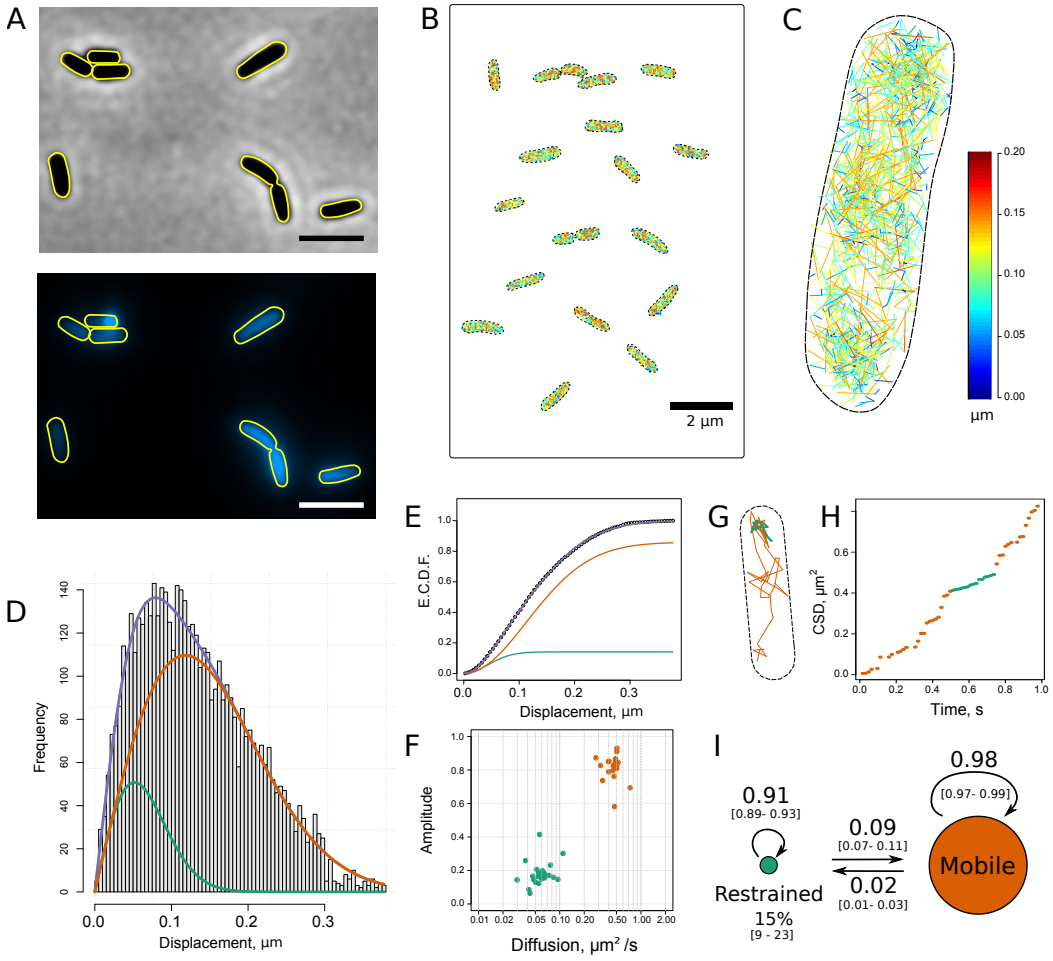

Fig. 2.
(A) Phase-contrast (upper) and fluorescence (lower) images of PAO1 PvdA-eGFP taken from Succinate Media cultures grown at 30℃ for 48 h. PvdA-eGFP is found homogeneously distributed in the cytoplasm. Some cells presented fluorescent spots at one pole, as previously described (23–25). Scale bars = 2 µm.
(B) Concatenated image of representative PvdA-PAmCherry cell diffusion maps obtained by sptPALM and (C) higher magnification of a representative single cell diffusion map. Trajectories steps are colour-coded to indicate instantaneous jump distances (µm) observed during Δt = 16ms time interval.
(D) Jump-distance distribution (JD) representing the Euclidean distance travelled by 23,800 PvdA-PAmCherry during a 16ms time interval. These data correspond to the JD observed in 29 cells measured of four independent experiments. (E) The corresponding empirical cumulative distribution function (ecdf) was fitted assuming a two-population diffusion model to retrieve diffusion coefficients of 0.06 [0.02 – 0.08] µm2/s and 0.47 [0.39 – 0.54] µm2/s (median [IQR]) determined at 20℃ for the restrained or bound (green) and mobile (orange) forms, respectively.
(F) Scatter plots of the amplitude of restrained and mobile forms of PvdA-PAmCherry as a function of their corresponding diffusion coefficients observed in 23 individual cells.
(G) Single PvdA-PAmCherry tracking trace observed at 62.5 Hz and (H) its cumulative square distance (CSD) as a function of time. Trace and CSD are colour-encoded according to their diffusing states as defined by a discrete two-state HMM model.
(I) Schematic representation of the probability transition matrix retrieved from the HMM. The diameters of the state circles are proportional to their corresponding steady-state amplitudes. The bootstrapped 2.5% and 97.5% percentiles of the transition matrix parameters are in squared brackets.

tion of PvdA-PAmCherry are photo-activated at each acquisition frame such that their localizations can be determined with sub-diffraction resolution. Thousands of sparse subsets of molecule coordinates pinpointed sequentially in time can then be accumulated within an imaged area. PvdA-PAmCherry was found to localize homogeneously in the cytoplasm. Despite a retrieved density of molecules of 2,000-3,000 localizations per μm^2, high enough to define spatial organization at the 40 nm resolution, no particular structural organization was observed for PvdA, at the exception of some preferential accumulation at one of the cell poles in some cells (23). We also used PALM to perform high-density single-particle tracking (sptPALM) to explore PvdA molecular trajectories within the cell. About 6,000 individual trajectories were computed from 54,000 linkable individual localizations in 42 cells, allowing the construction of single molecule diffusion maps at the single cell level. Diffusion patterns appeared very similar from cell to cell (Figure 2B), with traces of heterogeneous velocities scattered in all the cytoplasm (Figure 2C). We were not able to identify exclusion cytoplasmic areas for PvdA. To take advantage of the large number of (short) trajectories obtained with PvdA-PAmCherry in live cells, we computed jump-distances (JD) defined as the distance travelled by a single molecule during a fixed time lag Δt (from 16 to 50 ms). Over the population of molecules, jump distance distribution reflects the fine features of the underlying diffusion mechanisms and/or the number of diffusing species (Figure 2 D). Again, jump-distance

histograms of PvdA were found very similar between the different cells. Assuming PvdA underwent Brownian motions, nice adjustment of the empirical cumulative distribution of the JD distribution was obtained with a two-population model (Figure 2E), suggesting the presence of two diffusing populations of PvdA. Diffusion coefficients were 0.06 [0.02; 0.08] $\mu m^2/s$ and 0.47 [0.39 – 0.54] $\mu m^2/s$, values we assigned to trapped and diffusing species, respectively (Figure 2 F). Due to the finite localization precision (localization error of $\sim$ 30-40 nm), PvdA diffusing at 0.06 $\mu m^2/s$ could indiscriminately correspond to trapped, restrained or immobile fractions of PvdA. This fraction was found to represent about 10 to 24% (median 15%) of the total PvdA. The value of 0.47 [0.39 – 0.54] $\mu m^2/s$ is about an order of magnitude slower as compared to the observed or calculated diffusion of free cytoplasmic proteins with the same molecular weight in *E. coli* (29). Although the viscosity of the cytoplasm of PA01 might be slightly increased due to its smaller volume and its bigger genome size as compared to *E. coli*, it is unlikely to explain such a difference. PvdA must thus diffuse in the cytoplasm bound to a large complex. To explore possible transitions occurring between these two population states, we adjusted the square displacement values with a discrete two-state hidden Markov models (HMM) assuming an exponential probability distribution for the observed squared displacements. The HMM provides information about the sequence of states, the duration time in a state before transition, the probabilities for molecules to transition from one state to the other, and mean diffusion values. A representative tracking trace (although much longer than the 128 ms median trace duration) is presented in Figure 2G for illustration, together with its cumulative square displacement (CSD) plotted over time (29), to provide a visual representation of the HMM model output. An overall linear increase of CSD for a given time window indicates jump-distances are distributed around its average value and that the molecule diffuses uniformly. Break points defined by changes in slopes correspond to state transitions. It is clearly illustrated in figure 2G that the colour-encoded HMM model properly identify the two states and their transitions. The transition probability matrix Pi of the model is presented in figure 2H from which the steady-state amplitudes of the two-populations was calculated as the marginal distribution of the stationary Markov chain. A value of 15% ($IC_{95\%} = [9;23]\%$) was associated to the constrained state, in very good agreement with the estimation made by fitting the JD ecdf. All these results were reproduced using PvdA-eYFP to rule out any quantification artifacts that would be due to PAmCherry photo-physical properties (see Figure S1).

Taken together, these data clearly demonstrate PvdA was mostly diffusing in the cytoplasm bound to large protein complex without evidence for any spatial organization pattern or cytoplasmic exclusion areas at a 40 nm resolution. A small fraction estimated at $\sim$ 15% exhibited reduced diffusion rate. We assigned it to a trapped or bound state. The diffusing and trapped fractions were found exchangeable with about 260 events of free-to-bound and bound-to-free transitions observed within traces.

PvdI interacts with several PvdA

PvdA is an ornithine hydroxylase (22) working in tandem with the hydroxyornithine transformylase PvdF (19) to generate fOH-Ornithine used as a building block by PvdI and PvdJ. To explore of whether NRPS are cytoplasmic partner of PvdA, we sought to explore the physical interactions between PvdA and PvdI in live cells producing PVD. We used fluorescence lifetime imaging microscopy (FLIM) to measure Förster resonance energy transfer (FRET). FLIM is a general technique to probe changes in fluorophores' local environment. In time-domain FLIM, a pulsed laser periodically excites the fluorophores in the sample. Following excitation, fluorophores relax into their ground state either by emitting a photon (radiative decay) or through a non-radiative pathway. The fluorescence lifetime τ is defined as the average time a fluorophore remains in the excited state after excitation according to

$$\tau = \frac{1}{k_r + k_{nr}} \quad \textbf{(1)}$$

in which k_r are the radiative and k_{nr} the non-radiative rate constants. Experimentally, each individual fluorescence photon detected is tagged with its arrival time relative to the last excitation laser pulse. The fluorescence lifetime τ can thus be retrieved by adjusting the experimental fluorescence decay with a sum of exponential defined by rates inversely proportional to their fluorescence lifetimes. In the presence of a fluorescence acceptor (as mCherry) in the very close vicinity of a fluorescence donor (as eGFP), fluorescence energy transfer (FRET) can occur - increasing the non-radiative de-excitation rate of the donor and thus decreasing its fluorescence lifetime. FRET can only occur if the acceptor is only few nm apart from the donor, a distance range implying physical interaction between the labelled molecules. FLIM FRET is thus particularly well suited to probe protein-protein interactions in living cells (27, 30, 31).

Strains expressing PvdA-eGFP or PvdI-eGFP cultured in succinate media for 48h were imaged using FLIM (Figure 3A). Their fluorescence decays were adjusted with a single exponential model to retrieve their mean fluorescence lifetime. The expression level of PvdA-eGFP, measured by the fluorescence intensity of cells on microscopy image, was higher than that of PvdI-eGFP (see supplementary Figure S2). But the mean fluorescence lifetimes of PvdA-eGFP or PvdI-eGFP were very similar with median values of about 2.2 ns (Figure 3 B-C). The fluorescence lifetime is an intrinsic parameter of the fluorophore that does not depend on the concentration. FRET FLIM is therefore more robust than intensity-based methods to measure FRET when the concentration of interacting partner cannot be controlled.

Co-expression of PvdI-mCherry with PvdA-eGFP resulted in a very limited shortening of the average lifetime (Figure 3 B-C). It suggests poor interaction or long inter-dyes distances. In sharp contrast, the mean lifetime of cells expressing PvdI-eGFP was significantly shortened in the strain in which PvdA-mCherry was co-expressed. The energy trans-

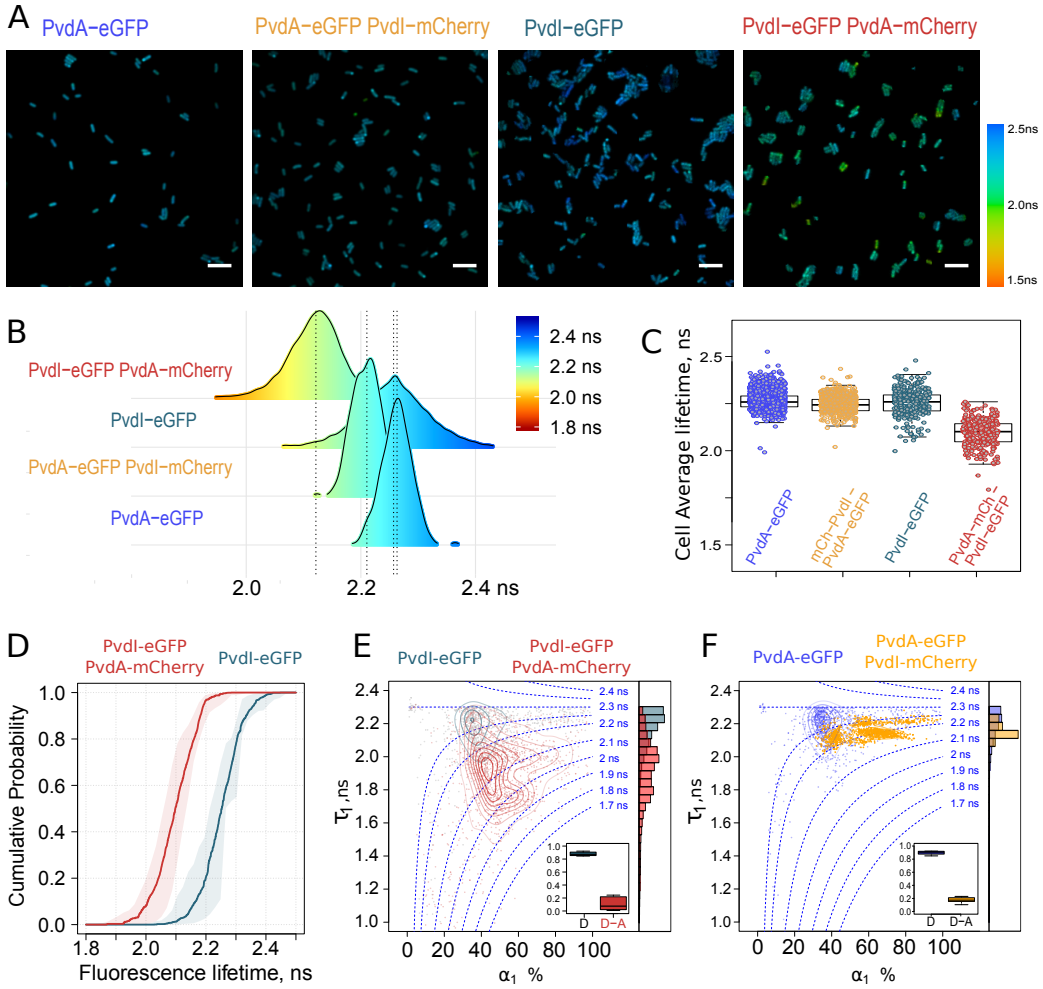

Fig. 3.
(A) Representative FLIM images of (from left to right) PvdA-eGFP, PvdA-eGFP PvdI-mCherry, PvdI-eGFP and PvdI-eGFP PvdA-mCherry strains, showing limited shortening in the average lifetime of PvdA-eGFP co-expressed with PvdI–mCherry in PaO1 but a larger effect for PvdI-eGFP co-expressed with PvdA-mCherry. All images are colour-encoded according to the pixel fluorescence lifetime values. The same colour scale (on the right) is used for the four images. Scale bar = 5 μm.
(B) Density of the mean fluorescence lifetime of pixels of (from bottom to top) PvdA-eGFP (n = 10,863), PvdA-eGFP PvdI-mCherry (n = 13,127), PvdI-eGFP (n = 6,962) and PvdI-eGFP PvdA-mCherry (n = 14,456) strains from at least N=3 independent experiments. (n = total number of pixels).
(C) Individual cell average fluorescence lifetime of (from left to right) PvdA-eGFP (ncell = 1,154; N=8), PvdA-eGFP PvdI-mCherry (ncell = 486; N=3), PvdI-eGFP (ncell = 291; N = 3) and PvdI-eGFP PvdA-mCherry (ncell = 303; N = 3). (ncell = number of analysed cells; N = number of independent experiments).
(D) Cumulative probability of the fluorescence lifetime of PvdI-eGFP and PvdI-eGFP PvdA-mCherry (data from panel B)
(A), (B), (C) and (D) provide evidence for a physical interaction between PvdA and PvdI.
(E) and (F) Density map with contour lines of (τ_1, α_1) fitting parameters (with τ_1 marginal distribution) showing clusters of pixels with similar decay signature for (E) PvdI-eGFP (grey) and PvdI-eGFP PvdA-mCherry (red) and (F) PvdA-eGFP (blue) and PvdA-eGFP PvdI-mCherry (orange). Inset: boxplot of the fraction of pixels with single exponential decay pixels - corresponding to decays with no energy transfer – for donor only (D) or donor-acceptor (D-A) conditions.

fer occurring between PvdI-eGFP and PvdA-mCherry can be seen by comparing the distribution of the average lifetime of pixels of PvdI-eGFP vs PvdI-eGFP PvdA-mCherry (Figure 3 B) and on their corresponding empirical cumulative distribution (Figure 3 D). It can also be seen by comparing the average lifetimes calculated for each individual cell (Figure 3 C). At the diffraction-limited resolution, the FRET signal is rather homogeneous in all the cytoplasm of a given cell. It seems unlikely that just swapping eGFP for mCherry and mCherry for eGFP have such a drastic effect on PvdA/PvdI interaction - and these two strains retain the ability of producing PVD with similar efficiencies. The apparent contradiction in the above findings can be reconciled regarding expression levels of the two proteins. Epi-fluorescence microscopy showed the cytoplasmic fluorescence intensity of strains expressing PvdA-eGFP was far higher than that of PvdI-eGFP strains (see supplementary Figure S2). Therefore, it can be envisioned PvdA-eGFP used as a donor would coexist as a minor fraction transferring energy to the mCherry and a major form free of transfer, both forms exhibiting different fluorescence lifetimes. Because the time resolved fluorescence decay spatially sums photons emitted by the different species, the resulting average fluorescence lifetime corresponds to a sum of (at least two) exponential weighted by their relative fluorescence. The fluorescence decay of PvdA-eGFP PvdI-mCherry will thus tends towards PvdA-eGFP de-

cay as the relative amount of non-transferring PvdA-eGFP increases. Similarly, the fluorescence decay of the complex labelled with mCherry on the protein with the higher stoichiometry will rapidly diverge from the fluorescence decay of the similar complex reversely labelled as the stoichiometry ratio increases. To take species mixture into account, fluorescence decays were fitted with a two-exponential component model in which the average lifetime is defined as a weighted sum of two decays according to

$$\langle\tau\rangle = \begin{pmatrix}\tau_1 & \tau_2\end{pmatrix}.\begin{pmatrix}\alpha_1 \\ \alpha_2\end{pmatrix} = \sum_{i=1}^{2}\alpha_i.\tau_i \qquad \textbf{(2)}$$

To limit over-fitting and improve fitting convergence, the long-lived lifetime τ_2 was fixed at the 90th percentile of PvdA-eGFP or PvdI-eGFP lifetimes defined using one single exponential decay (2.25 - 2.30 ns), whereas the lifetime value of the fast decay τ_1 and the relative contribution of each component defined by α_1 and α_2 could float. For a two-component model α_2=1- α_1 and $\langle\tau\rangle$ can thus be rewritten as

$$\langle\tau\rangle = \tau_2 - \alpha_1.(\tau_2 - \tau_1) \qquad \textbf{(3)}$$

A successful fit procedure will converge toward $\langle\tau\rangle$ by adjusting τ_1 and α_1 and will provide τ_1 and α_1 conditional probability distributions given the fixed τ_2 value. A plot of τ_1 as a function of α_1 can be drawn as a diagram to represent observations made over all fitted pixels. An estimation of the 2D density of the pixel spatial distribution in this plot provides an estimation of the average lifetime (centre of the density map contour plot) but also the bivariate distribution of (τ_1, α_1) parameters. As compared to PvdI-eGFP, the distribution of (τ_1, α_1) measurements of PvdI-eGFP PvdA-mCherry was much more scattered, with a significant part of the distribution showing shortened τ_1 with values ranging from about 2.2 ns down to 1.6 ns (Figure 3 E). It corresponded to large changes in the fluorescence decay parameters and sustained pronounced energy transfer between the two fluorophores. The fraction of pixels with one single fluorescence lifetime component were also dropped from about 85% to about 10% (Figure 3 E inset). These FLIM data clearly showed PvdA is physically interacting with PvdI.

In sharp contrast, the (τ_1, α_1) distribution of PvdA-eGFP PvdI-mCherry was mostly positioned in area corresponding to an average lifetime of about 2.2 ns. Only about 50% of the fitted pixels were better described with a two-component decay, and τ_1 values were only slightly shortened to about 2.1 ns.

If equimolar complex were formed for PvdI-PvdA complexes, the two (τ_1, α_1) maps for PvdI-eFGP PvdA-mCherry and PvdA-eGFP / PvdI-mCherry would look very similar, only being shifted along the α_1 axis due to the difference in the relative amount of energy transferring species. Indeed, due to the difference in the expression level of the two enzymes, almost all the PvdI molecules would be bound to PvdA (high value for α_1) while only a small fraction of PvdA would be bound on PvdI (low value of α_1) but in both cases τ_1 would not be affected because the structure of the interacting complex would remain unchanged. Our observations largely differed from this situation with τ_1 values being also affected (much shorter τ_1 values are observed for mCherry tagged PvdA - compare red contour lines in Figure 3E and orange ones in Figure 3 F). The latter is likely explained by the presence of multiple acceptors, further shortening the average lifetime according to

$$\langle\tau\rangle = \left(1/\tau + \sum_{i=1}^{n} k_i.\tau_i\right)^{-1} \qquad \textbf{(4)}$$

in which n is the number of acceptors with properties k_i and τ_i , the transfer rates and donor lifetimes, respectively. One can thus infer multiple PvdA-mCherry are bound on average to PvdI-eGFP NRPS.

Taken together, these observations provide evidence for a physical interaction between PvdA and PvdI and suggest multiple PvdA are bound to one molecule of PvdI.

PvdA interacts with PvdJ

PvdJ also contains a module responsible for the addition of L-fOH-Ornithine in the pyoverdine peptide. We decided to monitor FLIM-FRET between PvdA and PvdJ (Figure 4 A). The mean lifetime of PvdJ-eGFP PvdA-mCherry estimated from a single exponential decay model was shortened by about 10-15% as compared to PvdJ-eGFP fluorescence lifetime with absolute values of about 2.0-2.1 ns (Figure 4A). As for PvdA-PvdI interaction, we could not define any spatial pattern of where the interaction takes place. Using a two-component fitting model, we observed the relative amount of PvdJ-eGFP undergoing energy transfer in the presence of PvdA-mCherry was close to 100% (Figure 4 B inset). But on the contrary to PvdI-eGFP, the distribution of τ_1 was modal at about 2.0 ns and very few shorter τ_1 values were observed. Interestingly, a similar value of τ_1 was observed for the fraction of PvdA-eGFP molecules interacting with PvdJ-mCherry, associated to a α_1 value of $\sim$ 40%. Therefore, the same τ_1 value was observed irrespective of the labelling scheme of the two enzymes. This signed the presence of a possibly unique binding site for PvdA on PvdJ that governs the interaction between PvdA and PvdJ. This conclusion is in line with a previous report showing by double-hybrid that PvdA interacts with PvdJ M2 isolated module (24) - the module responsible for incorporation of formyl-OHOrn (Figure 1 C). The high value of α_1 observed for PvdJ-eGFP PvdA-mCherry indicated that in the cellular context, the binding site of PvdJ is saturated by PvdA – although we cannot discriminate between a strong affinity site with long residency time of PvdA on PvdJ or a situation of fast exchange of PvdA molecules on this binding site.

PvdA interacts with PvdL and PvdD in cells

We further investigated the interaction of PvdA with PvdL and PvdD. None of these two NRPS are using PvdA product as a building block. We were nevertheless able to evidence physical interactions between PvdA and PvdL (Figure

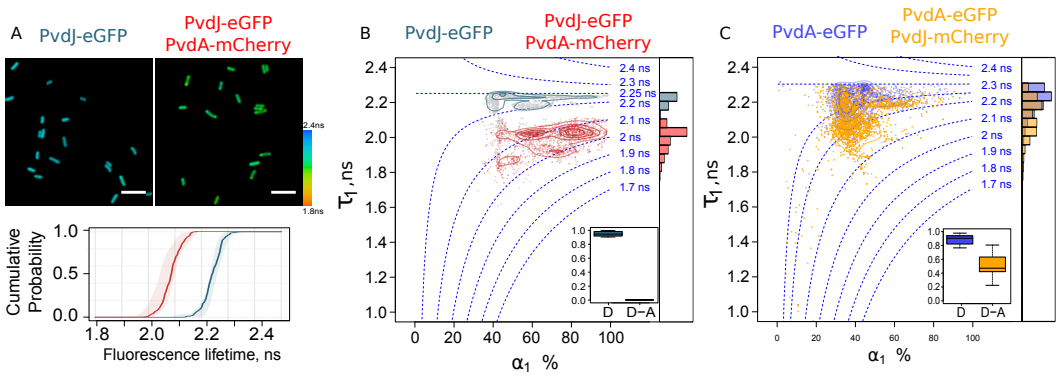

Fig. 4.
(A) Representative FLIM images of PvdJ-eGFP and PvdJ-eGFP PvdA strains, showing the shortening in the average lifetime of PvdJ-eGFP co-expressed with PvdA–mCherry in live PAO1. The cumulative probability of the fluorescence lifetime of these two strains demonstrate the interaction in live cell of PvdA with PvdJ with an energy transfer of about 10-15%.
(B) Density map with contour lines of (τ_1, α_1) fitting parameters of PvdJ-eGFP (grey) and PvdJ-eGFP PvdA-mCherry (red).
(C) Density map with contour lines of (τ_1, α_1) fitting parameters of PvdA-eGFP (blue) and PvdA-eGFP PvdJ-mCherry (orange).
(B) and (C) provide evidence for a major and possibly unique binding site for PvdA on PvdJ

5) and between PvdA and PvdD (Figure 6). Looking at figure 5 and 6, it clearly appears that the binding mode of PvdA to PvdL differed from the one of PvdA to PvdD. It is also very striking that results observed for PvdL were very similar to that observed for PvdI – with the slight difference of a lower affinity that results in a smaller fraction of interacting species explaining a smaller effect on shortening the average lifetime. On the other hand, the observations made for PvdD were broadly like PvdJ with a significant amount of interacting eGFP-PvdD characterized by a τ_1 value of about 2.0 ns – the same τ_1 value than that measured for the small fraction of PvdA-eGFP interacting with mCherry-PvdD. But on the contrary to PvdJ, a second binding site with shorter τ_1 value (about 1.8 ns) was also present – suggesting PvdD can accommodate more than one PvdA.

Discussion

In this work, we constructed PAO1 strains with genes coding for PvdA and NRPS fluorescent proteins (see supplementary table 1) inserted at the chromosomal level. These tagged-enzymes retained the expression levels and functions of the endogenous ones. We used these strains to explore interactions between four NRPS responsible for the biosynthesis of the PVD peptidic backbone and PvdA, a tailoring enzyme also involved in the PVD biosynthesis pathway. We found that PvdA was not existing as a free protein in the cytoplasm but was engaged in large complexes. We inferred from FLIM data about the physical interactions of PvdA with PvdI and PvdJ but also with PvdL and PvdD to demonstrate different binding modes of PvdA on the different NRPS.
Interestingly, the interaction of PvdA with PvdI and with PvdJ, the two NRPS using fOHOrn as a building block, were largely different in extent and nature. The presence of several binding sites of relatively low affinity has to be considered to explain our FLIM observations with PvdI. The interactions of several PvdA with PvdI may fulfill the necessity for an excess of substrate locally available to optimize the activity of NRPS enzymes. An unbalanced binding stoichiometry must also compensate fOHOrn dilution in the cytoplasm of the cell. On the contrary, a major binding site for PvdA was found on PvdJ. The M2 module previously identified by two-hybrid as an interacting partner of PvdA (24) and responsible for fOHOrn insertion is a good candidate to harbour this binding site for PvdA. The difference of binding mechanism of the two NRPS is nevertheless striking. Based on the fact that PvdL has a global binding behaviour very similar to PvdI, the molecular size of the NRPS could be an element explaining this binding mode – the larger the NRPS the higher the number of PvdA binding site the enzyme can accommodate. But some additional speculation can be made. We would for example propose to make the connection between (i) the conserved position of fOH-Orn in the PVD sequence of *Pseudomoas aeruginosa* and (ii) the presence of a single or multiple binding sites. Indeed, the module 2 of PvdJ is well conserved. On the opposite, the insertion of the fOH ornithine by PvdI is more variable, with position corresponding to module 2, 3 or 4 of PvdI in the different *P. aeruginosa* strains (6, 32) (*P. aeruginosa* strains are able to produce three different pyoverdines, PVDI, PVDII and PVDIII with a different peptide sequence). In this context, evolving multiple binding sites even with low affinities outside the modules provide the necessary flexibility to ensure product produced by PvdA to be available whatever the fOH ornithine module position. It suggests additionally that rather than physical coordination between active sites of tailoring enzymes and NRPS modules, only co-localization of sequential enzymes seems to be enough to promote metabolic efficiency. Taken together, we can then envisage binding sites have co-evolved with module specificity.

FLIM-FRET method is largely used to quantify protein-protein interactions. We demonstrated here that FLIM can be also used as a valuable tool for the quantification and characterization of heterogeneous interacting complex in living bacteria. The approach reported in Figure 3 or Figure 4 allowed to explore fluorescence signatures with the advantage of more clearly visualizing heterogeneities to provide key in-

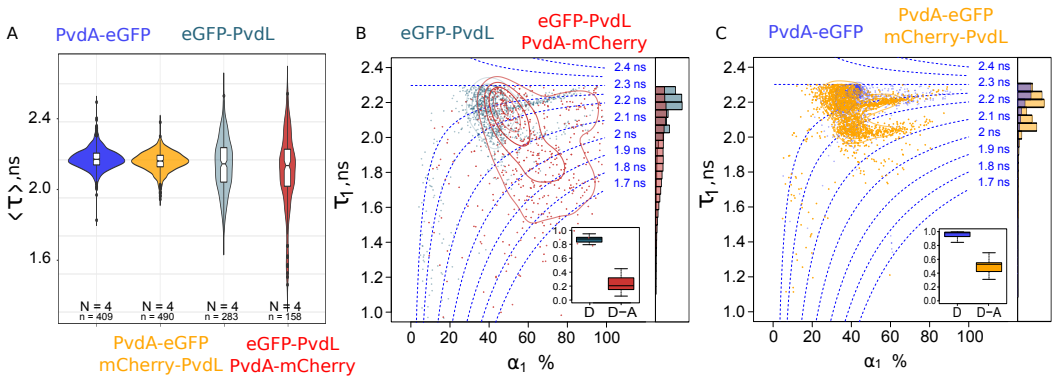

Fig. 5.
(A) Violin pot of the fluorescence lifetime of PvdA-eGFP (blue), PvdA-eGFP mCherry-PvdL (orange), eGFP-PvdL (grey) and eGFP-PvdL PvdA-mCherry (red) showing a very small decrease of the averaged fluorescence lifetime of eGFP-PvdL PvdA-mCherry as compared to eGFP-PvdL.
(B) Density map with contour lines of (τ_1, α_1) fitting parameters of eGFP-PvdL (grey) and eGFP-PvdL PvdA-mCherry (red).
(C) Density map with contour lines of (τ_1, α_1) fitting parameters of PvdA-eGFP (blue) and PvdA-eGFP mCherry-PvdL (orange).
(B) and (C) provide evidence for multiple binding sites of low affinity for PvdA on PvdL.

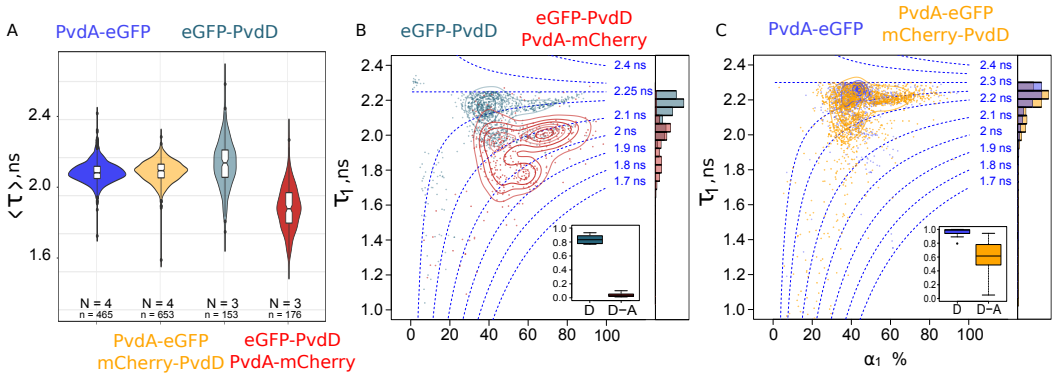

Fig. 6.
(A) Violin pot of the fluorescence lifetime of PvdA-eGFP (blue), PvdA-eGFP mCherry-PvdD (orange), eGFP-PvdD (grey) and eGFP-PvdD PvdA-mCherry (red) showing a shortening of the averaged fluorescence lifetime of eGFP-PvdD when interacting with PvdA-mCherry
(B) Density map with contour lines of (τ_1, α_1) fitting parameters of eGFP-PvdD (grey) and eGFP-PvdD PvdA-mCherry (red).
(C) Density map with contour lines of (τ_1, α_1) fitting parameters of PvdA-eGFP (blue) and PvdA-eGFP mCherry-PvdD (orange).
(B) and (C) provide evidence, as for PvdJ, for a major binding site for PvdA on PvdD, with a possible second binding site of lower affinity.

formation about the FRET extend occurring between eGFP and mCherry. In PAO1 cultured in iron-deprived succinate media, the expression of PvdA is far higher than that of the different NRPS. Based on different FRET distributions between strains expressing PvdA tagged with the fluorescent donor (PvdA-eGFP) as compared to strains expressing PvdA-mCherry tagged with the acceptor, we evidence the presence of physical interaction between PvdA and NRPS in complex in which transferring and non-transferring bound PvdA coexist. We were also able to evidence the presence of multiple PvdA bound simultaneously on some NRPS and clearly distinguish this situation from complexes with 1:1 stoichiometry.

Although we did not interrogate direct interactions between the different NRPS in this work, our findings provide strong evidence for siderosomes. Such organization has been previously hypothesized based on biochemical observation, but the difficulty to handle these complexes limits their *in vitro* explorations. The binding mode of PvdA onto NRPS can explain why only tiny amounts of NRPS were captured in protein pull-down assay using 6His-PvdA as bait (24). Even though very low amount of NRPS were captured compared to their levels in the flow-through fraction, PvdI and PvdL were the two NRPS the most retained (as compared to PvdD and PvdJ) – likely because these are the two NRPS able to accommodate the higher number of binding sites.

Taken together, our data clearly provide evidence that secondary metabolite pathways are much more organized than initially envisioned, with multiple interactions and multiple binding modes occurring between accessory proteins and NRPS. If clustering of all the PVD bio-synthesis machinery in a single complex is possibly increasing the synthesis efficiency, notably by sequestrating intermediate products, the understanding of how metabolic enzymes interact and coordinate with each other in space and time to ensure their metabolic functions is mostly at its infancy2. Reversible spatial assemblies of sequential metabolic enzymes have been proposed as a general mechanism able to regulate metabolic activities, including in eukaryotes (4, 33) , but they remain highly challenging to investigate in real time in the cellular context.

Due to their non-vital nature and their experimentally tractable expression, siderosomes are good candidates to be used as model systems to demonstrate the functional signifi-

cance of highly orchestrated enzyme organizations in the cellular context. Our data demonstrate these complexes can be directly characterized in the cellular environment in live cells. Many questions about siderosomes are still waiting for answers. Do and how NRPS interact witch each other? Are siderosome interacting with the inner membrane and therefore can it be considered as metabolons? What is the role of the myristic chain present in the PVD precursor and removed once this precursor has reached the bacterial periplasm (34)? Additional general knowledge gained from siderosome will likely contribute further to the general understandings of mechanisms ruling widespread metabolic pathways cellular organisations.

Material and Methods

Bacterial strains, plasmids and growth conditions

P. aeruginosa strains used in this study are listed in Table S1. Bacteria were grown in 5mL lysogeny broth [(LB); Difco] at 30°C under 220 rpm orbital shaking. To induce the expression of the pyoverdine biosynthesis pathway enzymes, *P. aeruginosa* strains were pelleted by centrifugation, washed and further grown overnight at 30°C in an iron-deficient succinate medium (composition: $6\,\mathrm{g/L}$ K_2HPO_4, $3\,\mathrm{g/L}$ KH_2PO_4, $1\,\mathrm{g/L}$ $(NH_4)_2SO_4$, $0.2\,\mathrm{g/L}$ $MgSO_4$, 7 H_2O and $4\,\mathrm{g/L}$ sodium succinate with the pH adjusted to 7.0 by adding NaOH). Cells were further diluted and grown an additional 24 hours. The presence of pyoverdine in the supernatant can be visually observed as an intense yellow-green water-soluble pigment.

Mutants construction

All enzymes for DNA manipulation were purchased from ThermoFisher Scientific and were used in accordance with the manufacturer's instructions. *E. coli* strain TOP10 (Invitrogen) was used as the host strain for all plasmids. The DNA fragments from *P. aeruginosa* used for cloning were amplified from the genomic DNA of the PAO1 strain with Phusion High-Fidelity DNA polymerase (ThermoFisher Scientific). The primers used are listed in supplementary Table S3 of the Supporting Information. As previously described (23), the general procedure for the construction of the plasmids involved insertion of the *mcherry*, *egfp* or *pamcherry* gene flanked by upstream and downstream regions of 700 bp, corresponding to the insertion site, into a pME3088 or a pEXG2 vector. Mutations in the chromosomal genome of *P. aeruginosa* were generated by transferring the suicide vector from E. coli TOP10 strain into the *P. aeruginosa* recipient strain and allowing the plasmid to integrate into the chromosome, with selection for tetracycline resistance for pME3088 (35) or gentamicin resistance for pEXG2. A second crossing-over event excising the vector was achieved by enrichment for tetracycline-sensitive cells (pME3088) or sucrose resistant cells selection (pEXG2), to generate the corresponding mutants (36). All tag insertion mutants were verified by PCR and sequencing.

Wide field imaging

Wide field imaging was performed on a Micro-Manager (37) controlled Olympus IX-81 inversed microscope equipped with z-drift control and auto-focus system (ZDC Olympus). Phase images were generated using a Phase3 100X 1.4NA objective (Olympus) using a 512×512 pixels EM-CCD (ImagEM - Hamamatsu Photonics - Japan). Epi-fluorescence excitation was provided by a 488 nm laser diode (spectra physics) using a 488 nm (Di01-R488 - Semrock) dichroic filter. Fluorescence signals were filtered using a 488 nm Long pass filter (BLP01-488R-25 – Semrock). Live-cells were immobilized on a 1% agarose pad and imaged at 20°C. Quantitative fluorescence measurements were performed at the cell level using a home-made imageJ plugin for cell segmentation and fluorescence quantification. Initial cell segmentation was based on a Laplacian of Gaussian (LoG) filtering of the phase image and further used to define a rod-shape contour (sphero-cylinder) based on different central moment calculations. Initial rod-shape contours were then refined based on the isotropic 3×3 gradient of the initial image to adjust bacteria contours.

PhotoActivated Localization Microscopy (PALM) and single particle tracking-PALM (sptPALM)

PALM and sptPALM (26) were performed on a home-built Micro-Manager (37) controlled inversed-microscope based on a Nikon Eclipse II equipped with a 100X 1.49 objective (Nikon - Japan) and a drift focus compensator (Perfect Focus System - Nikon -Japan). Photoactivable mCherry (PA-mCherry) was excited with a 561 nm diode laser (Oxxius -France) and activated with a 405 nm laser diode (Spectra Physics - Germany) selected by an acousto-optic tunable filter (AOTFnC 400-650 TN, AA Otpo Electronic- France). Fluorescence emission of PA-mCherry was collected through a quadri-band dichroic filter (FF405/496/560/651-Di01-25x36 - Semrock - USA) and further filtered with a LP-561 nm long-pass filter (Chroma - Germany). The wavefront distortions of the emission signal were corrected using an adaptive optics device (MicAO, Imaging Optics - France) before being imaged on a 512×512 pixels EM-CCD (ImagEM - Hamamatsu Photonics - Japan) operating at -65°C with an ADU to photon conversion factor of about 60. Image stacks ranging from 2000 to 5000 frames with an exposure time of 16 to 50 ms were typically recorded for sptPALM using a home-written Beanshell acquisition script. Molecules localizations were retrieved using Peakfit, an open source software package for Fiji and further analysed using self-written script in R. Tracking traces were generated using the simple Linear Assignment Problem (LAP) tracker (38) implemented in TrackMate plugin (39) for Fiji. The simple LAP is well suited for tracking molecules undergoing Brownian motion or for low density of molecules undergoing non-Brownian motion. Data were further analyzed in R according to a jump distance analysis (40) assuming the mean square displacement is proportional to the two-dimensional diffusion coefficient D (in $\mu\mathrm{m}^2/\mathrm{s}$) (2-D Brownian motion) such that $\langle r^2(\Delta t)\rangle = 4D_j\Delta t$. Diffusion coefficients were retrieved from the empirical cumulative distribution function (ecdf) of the particles' displacements in a set time interval according

to :

$$P(r^2, \Delta t) = 1 - \sum_{j=1}^{m} f_j . e^{-\frac{r^2}{4.D_j.\Delta t}} \quad \textbf{(5)}$$

The choice of fitting the ecdf instead of the discrete probability density function (pdf) histogram for fitting was motivated by the dependence of the pdf histogram to the user input for bin-size selection - possibly biasing the fitting parameters.
Hidden Markov model estimates were obtained using the Baum-Welch algorithm (41) and the Viterbi algorithm (42), both implemented in the R hmm package (https://cran.r-project.org/package=HMM) that predict the most likely sequence of Markov states given the observed data-set. Diffusion coefficients were obtained from the HMM exponential rates. HMM parameter confidence intervals (exponential rates and transition matrix) were obtained by bootstrap.
The tracking analysis procedure was challenged using data of the Particle Tracking Challenge (http://www.bioimageanalysis.org/track/) found in Supplementary Video 1 of reference (43) corresponding to simulated images of vesicles undergoing Brownian motions with medium particle density and a signal-to-noise ratio of four. Retrieved parameters were in excellent agreement with the ground truth as shown in Supplementary Figure S4.

Fluorescence Lifetime Imaging Microscopy (FLIM)
Time-correlated single-photon counting FLIM measurements were performed on a home-made two-photon excitation scanning microscope based on an Olympus IX70 inverted microscope with an Olympus 60× 1.2NA water immersion objective operating in de-scanned fluorescence collection mode (44, 45). Two-photon excitation at 930 nm was provided by a Ti:Sapphire oscillator (Mai Tai® DeepSee™, Spectra Physics - 80 MHz repetition rate, ≈ 70 fs pulse width) at 10-20mW. Fluorescence photons were collected through a 680 nm short pass filter (F75-680, AHF, Germany) and a 525/50 nm band-pass filter (F37-516, AHF, Germany) and directed to a fibre-coupled avalanche photodiode (SPCM-AQR-14-FC, Perkin Elmer) connected to a time-correlated single photon counting (TCSPC) module (SPC830, Becker & Hickl, Germany). Cells grown for 48h in succinate media were immobilized on a 1% agarose pad and rapidly imaged. Typically, area of 50×50 µm in the samples were scanned at 4 µs/pixel (1024×1024 pixels) for 100 s to 600 s to reach the Nyquist-Shannon sampling criteria and to achieve the appropriate photon statistics to investigate the fluorescence decays. Fluorescence decays were processed using a commercial software package (SPCImage V2.8, Becker & Hickl, Germany). A binning of two was applied before processing the fluorescence decays. FLIM data were further analyzed using a homemade ImageJ plugin and R scripts.

Funding information

This work was funded by Fondation pour la Recherche en Chimie (https://icfrc.fr/). The funders had no role in study design, data collection and interpretation, or the decision to submit the work for publication.

ACKNOWLEDGEMENTS
We acknowledge Dr Ludovic Richert for his valuable assistance on FLIM data acquisition and for the technical maintenance and development of the FLIM setup.

Bibliography

1. Pablo Meyer, Guillermo Cecchi, and Gustavo Stolovitzky. Spatial localization of the first and last enzymes effectively connects active metabolic pathways in bacteria. *BMC systems biology*, 8(1):131, dec 2014. ISSN 1752-0509. doi: 10.1186/s12918-014-0131-1.
2. Danielle L Schmitt and Songon An. Spatial Organization of Metabolic Enzyme Complexes in Cells. *Biochemistry*, 56(25):3184–3196, 2017. ISSN 1520-4995. doi: 10.1021/acs.biochem.7b00249.
3. Rammohan Narayanaswamy, Matthew Levy, Mark Tsechansky, Gwendolyn M Stovall, Jeremy D O'Connell, Jennifer Mirrielees, Andrew D Ellington, and Edward M Marcotte. Widespread reorganization of metabolic enzymes into reversible assemblies upon nutrient starvation. *Proceedings of the National Academy of Sciences of the United States of America*, 106(25):10147–52, jun 2009. ISSN 1091-6490. doi: 10.1073/pnas.0812771106.
4. Songon An, Ravindra Kumar, Erin D Sheets, and Stephen J Benkovic. Reversible compartmentalization of de novo purine biosynthetic complexes in living cells. *Science (New York, N.Y.)*, 320(5872):103–6, apr 2008. ISSN 1095-9203. doi: 10.1126/science.1152241.
5. Michele Castellana, Maxwell Z Wilson, Yifan Xu, Preeti Joshi, Ileana M Cristea, Joshua D Rabinowitz, Zemer Gitai, and Ned S Wingreen. Enzyme clustering accelerates processing of intermediates through metabolic channeling. *Nature biotechnology*, 32(10):1011–8, oct 2014. ISSN 1546-1696. doi: 10.1038/nbt.3018.
6. Jean-Marie M Meyer. Pyoverdines: pigments, siderophores and potential taxonomic markers of fluorescent Pseudomonas species. *Archives of microbiology*, 174(3):135–42, sep 2000. ISSN 0302-8933. doi: 10.1007/s002030000188.
7. Jacques Ravel and Pierre Cornelis. Genomics of pyoverdine-mediated iron uptake in pseudomonads. *Trends in microbiology*, 11(5):195–200, may 2003. ISSN 0966-842X.
8. C Georges and J M Meyer. High-molecular-mass, iron-repressed cytoplasmic proteins in fluorescent Pseudomonas: potential peptide-synthetases for pyoverdine biosynthesis. *FEMS microbiology letters*, 132(1-2):9–15, oct 1995. ISSN 0378-1097.
9. D E Lehoux, F Sanschagrin, and R C Levesque. Genomics of the 35-kb pvd locus and analysis of novel pvdIJK genes implicated in pyoverdine biosynthesis in Pseudomonas aeruginosa. *FEMS microbiology letters*, 190(1):141–6, sep 2000. ISSN 0378-1097.
10. Dimitris Mossialos, Urs Ochsner, Christine Baysse, Patrice Chablain, Jean-Paul Pirnay, Nico Koedam, Herbert Budzikiewicz, Diana Uría Fernández, Mathias Schäfer, Jacques Ravel, and Pierre Cornelis. Identification of new, conserved, non-ribosomal peptide synthetases from fluorescent pseudomonads involved in the biosynthesis of the siderophore pyoverdine. *Molecular microbiology*, 45(6):1673–85, sep 2002. ISSN 0950-382X.
11. David F Ackerley, Tom T Caradoc-Davies, and Iain L Lamont. Substrate specificity of the nonribosomal peptide synthetase PvdD from Pseudomonas aeruginosa. *Journal of bacteriology*, 185(9):2848–55, may 2003. ISSN 0021-9193.
12. Iain L Lamont and Lois W Martin. Identification and characterization of novel pyoverdine synthesis genes in Pseudomonas aeruginosa. *Microbiology (Reading, England)*, 149(Pt 4):833–42, apr 2003. ISSN 1350-0872. doi: 10.1099/mic.0.26085-0.
13. Matthias Strieker, Alan Tanović, and Mohamed A Marahiel. Nonribosomal peptide synthetases: structures and dynamics. *Current opinion in structural biology*, 20(2):234–40, apr 2010. ISSN 1879-033X. doi: 10.1016/j.sbi.2010.01.009.
14. Robert Finking and Mohamed A Marahiel. Biosynthesis of nonribosomal peptides1. *Annual review of microbiology*, 58:453–88, 2004. ISSN 0066-4227. doi: 10.1146/annurev.micro.58.030603.123615.
15. Mohamed A. Marahiel, Torsten Stachelhaus, and Henning D. Mootz. Modular Peptide Synthetases Involved in Nonribosomal Peptide Synthesis. *Chemical reviews*, 97(7):2651–2674, nov 1997. ISSN 1520-6890.
16. Andrew M Gulick. Nonribosomal peptide synthetase biosynthetic clusters of ESKAPE pathogens. *Natural product reports*, 34(8):981–1009, aug 2017. ISSN 1460-4752. doi: 10.1039/c7np00029d.
17. Yi-Ming Chiang, Shu-Lin Chang, Berl R Oakley, and Clay C C Wang. Recent advances in awakening silent biosynthetic gene clusters and linking orphan clusters to natural products in microorganisms. *Current opinion in chemical biology*, 15(1):137–43, feb 2011. ISSN 1879-0402. doi: 10.1016/j.cbpa.2010.10.011.
18. P Visca, A Ciervo, and N Orsi. Cloning and nucleotide sequence of the pvdA gene encoding the pyoverdin biosynthetic enzyme L-ornithine N5-oxygenase in Pseudomonas aeruginosa. *Journal of bacteriology*, 176(4):1128–40, 1994. ISSN 0021-9193.
19. B J McMorran, H M Shanta Kumara, K Sullivan, and I L Lamont. Involvement of a transformylase enzyme in siderophore synthesis in Pseudomonas aeruginosa. *Microbiology (Reading, England)*, 147(Pt 6):1517–24, jun 2001. ISSN 1350-0872. doi: 10.1099/00221287-147-6-1517.
20. H Ikai and S Yamamoto. Identification and analysis of a gene encoding L-2,4-diaminobutyrate:2-ketoglutarate 4-aminotransferase involved in the 1,3-diaminopropane production pathway in Acinetobacter baumannii. *Journal of bacteriology*, 179(16):5118–25, aug 1997. ISSN 0021-9193.
21. Li Ge and Stephen Y K Seah. Heterologous expression, purification, and characterization of an l-ornithine N(5)-hydroxylase involved in pyoverdine siderophore biosynthesis in Pseudomonas aeruginosa. *Journal of bacteriology*, 188(20):7205–10, oct 2006. ISSN 0021-9193. doi: 10.1128/JB.00949-06.
22. Kathleen M Meneely, Eric W Barr, J Martin Bollinger, and Audrey L Lamb. Kinetic mechanism of ornithine hydroxylase (PvdA) from Pseudomonas aeruginosa: substrate triggering of O2 addition but not flavin reduction. *Biochemistry*, 48(20):4371–6, may 2009. ISSN 1520-4995. doi: 10.1021/bi900442z.
23. Laurent Guillon, Maher El Mecherki, Stephan Altenburger, Peter L. Graumann, and Isabelle J. Schalk. High cellular organization of pyoverdine biosynthesis in Pseudomonas

aeruginosa: Clustering of PvdA at the old cell pole. *Environmental Microbiology*, 14(8): 1982–1994, 2012. ISSN 14622912. doi: 10.1111/j.1462-2920.2012.02741.x.

24. Francesco Imperi and Paolo Visca. Subcellular localization of the pyoverdine biogenesis machinery of Pseudomonas aeruginosa: a membrane-associated "siderosome". *FEBS letters*, 587(21):3387–91, nov 2013. ISSN 1873-3468. doi: 10.1016/j.febslet.2013.08.039.
25. Véronique Gasser, Laurent Guillon, Olivier Cunrath, and Isabelle J Schalk. Cellular organization of siderophore biosynthesis in Pseudomonas aeruginosa: Evidence for siderosomes. *Journal of inorganic biochemistry*, 148:27–34, jul 2015. ISSN 1873-3344. doi: 10.1016/j.jinorgbio.2015.01.017.
26. Suliana Manley, Jennifer M Gillette, George H Patterson, Hari Shroff, Harald F Hess, Eric Betzig, and Jennifer Lippincott-Schwartz. High-density mapping of single-molecule trajectories with photoactivated localization microscopy. *Nature methods*, 5(2):155–7, feb 2008. ISSN 1548-7105. doi: 10.1038/nmeth.1176.
27. P I Bastiaens and A Squire. Fluorescence lifetime imaging microscopy: spatial resolution of biochemical processes in the cell. *Trends in cell biology*, 9(2):48–52, feb 1999. ISSN 0962-8924.
28. Eric Betzig, George H Patterson, Rachid Sougrat, O Wolf Lindwasser, Scott Olenych, Juan S Bonifacino, Michael W Davidson, Jennifer Lippincott-Schwartz, and Harald F Hess. Imaging intracellular fluorescent proteins at nanometer resolution. *Science (New York, N.Y.)*, 313:1642–1645, 2006. ISSN 0036-8075. doi: 10.1126/science.1127344.
29. Tomasz Kalwarczyk, Marcin Tabaka, and Robert Holyst. Biologistics—Diffusion coefficients for complete proteome of Escherichia coli. *Bioinformatics*, 28(22):2971–2978, nov 2012. ISSN 1460-2059. doi: 10.1093/bioinformatics/bts537.
30. Prabuddha Sengupta and Jennifer Lippincott-Schwartz. Quantitative analysis of photoactivated localization microscopy (PALM) datasets using pair-correlation analysis. *BioEssays : news and reviews in molecular, cellular and developmental biology*, 34(5):396–405, may 2012. ISSN 1521-1878. doi: 10.1002/bies.201200022.
31. R N Day, A Periasamy, and F Schaufele. Fluorescence resonance energy transfer microscopy of localized protein interactions in the living cell nucleus. *Methods (San Diego, Calif.)*, 25(1):4–18, sep 2001. ISSN 1046-2023. doi: 10.1006/meth.2001.1211.
32. S Kilz, C Lenz, R Fuchs, and H Budzikiewicz. A fast screening method for the identification of siderophores from fluorescent Pseudomonas spp. by liquid chromatography/electrospray mass spectrometry. *Journal of mass spectrometry : JMS*, 34(4):281–90, apr 1999. ISSN 1076-5174. doi: 10.1002/(SICI)1096-9888(199904)34:4<281::AID-JMS750>3.0.CO;2-M.
33. Jarrod B French, Sara A Jones, Huayun Deng, Anthony M Pedley, Doory Kim, Chung Yu Chan, Haibei Hu, Raymond J Pugh, Hong Zhao, Youxin Zhang, Tony Jun Huang, Ye Fang, Xiaowei Zhuang, and Stephen J Benkovic. Spatial colocalization and functional link of purinosomes with mitochondria. *Science (New York, N.Y.)*, 351(6274):733–7, feb 2016. ISSN 1095-9203. doi: 10.1126/science.aac6054.
34. Mélissa Hannauer, Mathias Schäfer, Françoise Hoegy, Patrick Gizzi, Patrick Wehrung, Gaëtan L A Mislin, Herbert Budzikiewicz, and Isabelle J. Schalk. Biosynthesis of the pyoverdine siderophore of Pseudomonas aeruginosa involves precursors with a myristic or a myristoleic acid chain. *FEBS letters*, 586(1):96–101, jan 2012. ISSN 1873-3468. doi: 10.1016/j.febslet.2011.12.004.
35. Christophe Voisard, Carolee T. Bull, Christoph Keel, Jacques Laville, Monika Maurhofer, Ursula Schnider, Genevive Dfago, and Dieter Haas. Biocontrol of Root Diseases byPseudomonas fluorescens CHA0: Current Concepts and Experimental Approaches. In *Molecular Ecology of Rhizosphere Microorganisms*, pages 67–89. Wiley-VCH Verlag GmbH, Weinheim, Germany. doi: 10.1002/9783527615810.ch6.
36. R W Ye, D Haas, J O Ka, V Krishnapillai, A Zimmermann, C Baird, and J M Tiedje. Anaerobic activation of the entire denitrification pathway in Pseudomonas aeruginosa requires Anr, an analog of Fnr. *Journal of bacteriology*, 177(12):3606–9, jun 1995. ISSN 0021-9193.
37. Arthur D Edelstein, Mark A Tsuchida, Nenad Amodaj, Henry Pinkard, Ronald D Vale, and Nico Stuurman. Advanced methods of microscope control using μManager software. *Journal of biological methods*, 1(2). ISSN 2326-9901. doi: 10.14440/jbm.2014.36.
38. Khuloud Jaqaman, Dinah Loerke, Marcel Mettlen, Hirotaka Kuwata, Sergio Grinstein, Sandra L Schmid, and Gaudenz Danuser. Robust single-particle tracking in live-cell time-lapse sequences. *Nature methods*, 5(8):695–702, aug 2008. ISSN 1548-7105. doi: 10.1038/nmeth.1237.
39. Jean-Yves Tinevez, Nick Perry, Johannes Schindelin, Genevieve M Hoopes, Gregory D Reynolds, Emmanuel Laplantine, Sebastian Y Bednarek, Spencer L Shorte, and Kevin W Eliceiri. TrackMate: An open and extensible platform for single-particle tracking. *Methods (San Diego, Calif.)*, 115:80–90, feb 2017. ISSN 1095-9130. doi: 10.1016/j.ymeth.2016.09.016.
40. Laura Weimann, Kristina a Ganzinger, James McColl, Kate L Irvine, Simon J Davis, Nicholas J Gay, Clare E Bryant, and David Klenerman. A quantitative comparison of single-dye tracking analysis tools using Monte Carlo simulations. *PloS one*, 8(5):e64287, jan 2013. ISSN 1932-6203. doi: 10.1371/journal.pone.0064287.
41. Leonard E. Baum, Ted Petrie, George Soules, and Norman Weiss. A Maximization Technique Occurring in the Statistical Analysis of Probabilistic Functions of Markov Chains. *The Annals of Mathematical Statistics*, 41(1):164–171, feb 1970. ISSN 0003-4851. doi: 10.1214/aoms/1177697196.
42. A. Viterbi. Error bounds for convolutional codes and an asymptotically optimum decoding algorithm. *IEEE Transactions on Information Theory*, 13(2):260–269, apr 1967. ISSN 0018-9448. doi: 10.1109/TIT.1967.1054010.
43. Nicolas Chenouard, Ihor Smal, Fabrice de Chaumont, Martin Maška, Ivo F Sbalzarini, Yuanhao Gong, Janick Cardinale, Craig Carthel, Stefano Coraluppi, Mark Winter, Andrew R Cohen, William J Godinez, Karl Rohr, Yannis Kalaidzidis, Liang Liang, James Duncan, Hongying Shen, Yingke Xu, Klas E G Magnusson, Joakim Jaldén, Helen M Blau, Perrine Paul-Gilloteaux, Philippe Roudot, Charles Kervrann, François Waharte, Jean-Yves Tinevez, Spencer L Shorte, Joost Willemse, Katherine Celler, Gilles P van Wezel, Han-Wei Dan, Yuh-Show Tsai, Carlos Ortiz de Solórzano, Jean-Christophe Olivo-Marin, and Erik Meijering. Objective comparison of particle tracking methods. *Nature methods*, 11(3):281–9, mar 2014. ISSN 1548-7105. doi: 10.1038/nmeth.2808.
44. Salah Edin El Meshri, Denis Dujardin, Julien Godet, Ludovic Richert, Christian Boudier, Jean Luc Darlix, Pascal Didier, Yves Mély, Hugues de Rocquigny, and Hugues de Rocquigny Salah E El Meshri, Denis Dujardin, Ludovic Richert ,Christian Boudier, Julien Godet, Jean Luc Darlix, Pascal Didier, Yves Mély. Role of the nucleocapsid domain in HIV-1 Gag oligomerization and trafficking to the plasma membrane: a fluorescence lifetime imaging microscopy investigation. *Journal of Molecular Biology*, 427(6 Pt B):1480–94, mar 2015. ISSN 1089-8638. doi: 10.1016/j.jmb.2015.01.015.
45. Julien Batisse, Santiago Xavier Guerrero, Serena Bernacchi, Ludovic Richert, Julien Godet, Valérie Goldschmidt, Yves Mély, Roland Marquet, Hugues de Rocquigny, and Jean-Christophe Paillart. APOBEC3G impairs the multimerization of the HIV-1 Vif protein in living cells. *Journal of virology*, 87(11):6492–506, jun 2013. ISSN 1098-5514. doi: 10.1128/JVI.03494-12.

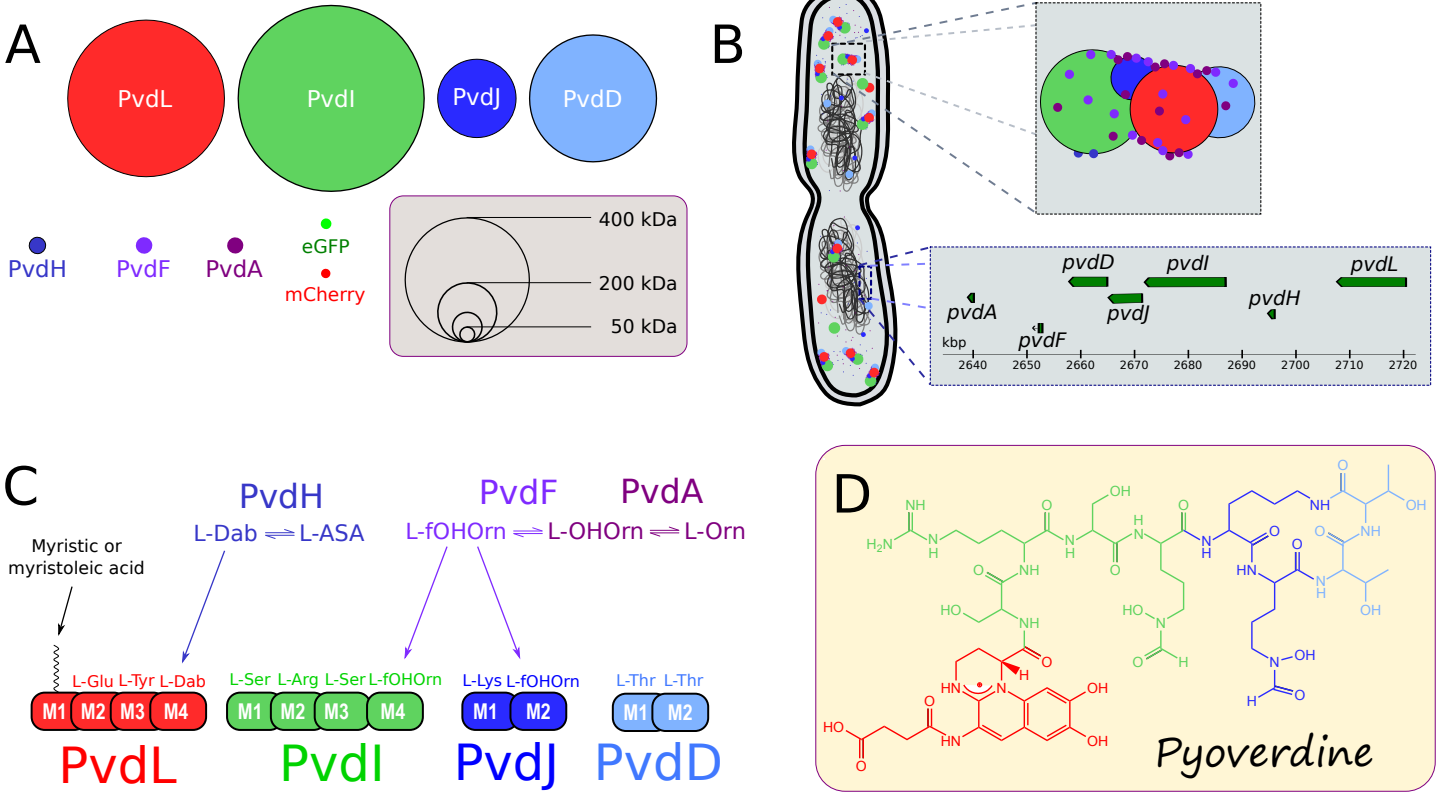
A
PvdL
PvdI
PvdJ
PvdD
PvdH
PvdF
PvdA
eGFP
mCherry
400 kDa
200 kDa
50 kDa
B
pvdD
pvdI
pvdL
pvdA
pvdJ
pvdH
pvdF
kbp
2640
2650
2660
2670
2680
2690
2700
2710
2720
C
PvdH
L-Dab ⇌ L-ASA
PvdF
PvdA
L-fOHOrn ⇌ L-OHOrn ⇌ L-Orn
Myristic or
myristoleic acid
L-Glu L-Tyr L-Dab
M1 M2 M3 M4
PvdL
L-Ser L-Arg L-Ser L-fOHOrn
M1 M2 M3 M4
PvdI
L-Lys L-fOHOrn
M1 M2
PvdJ
L-Thr L-Thr
M1 M2
PvdD
D
Pyoverdine

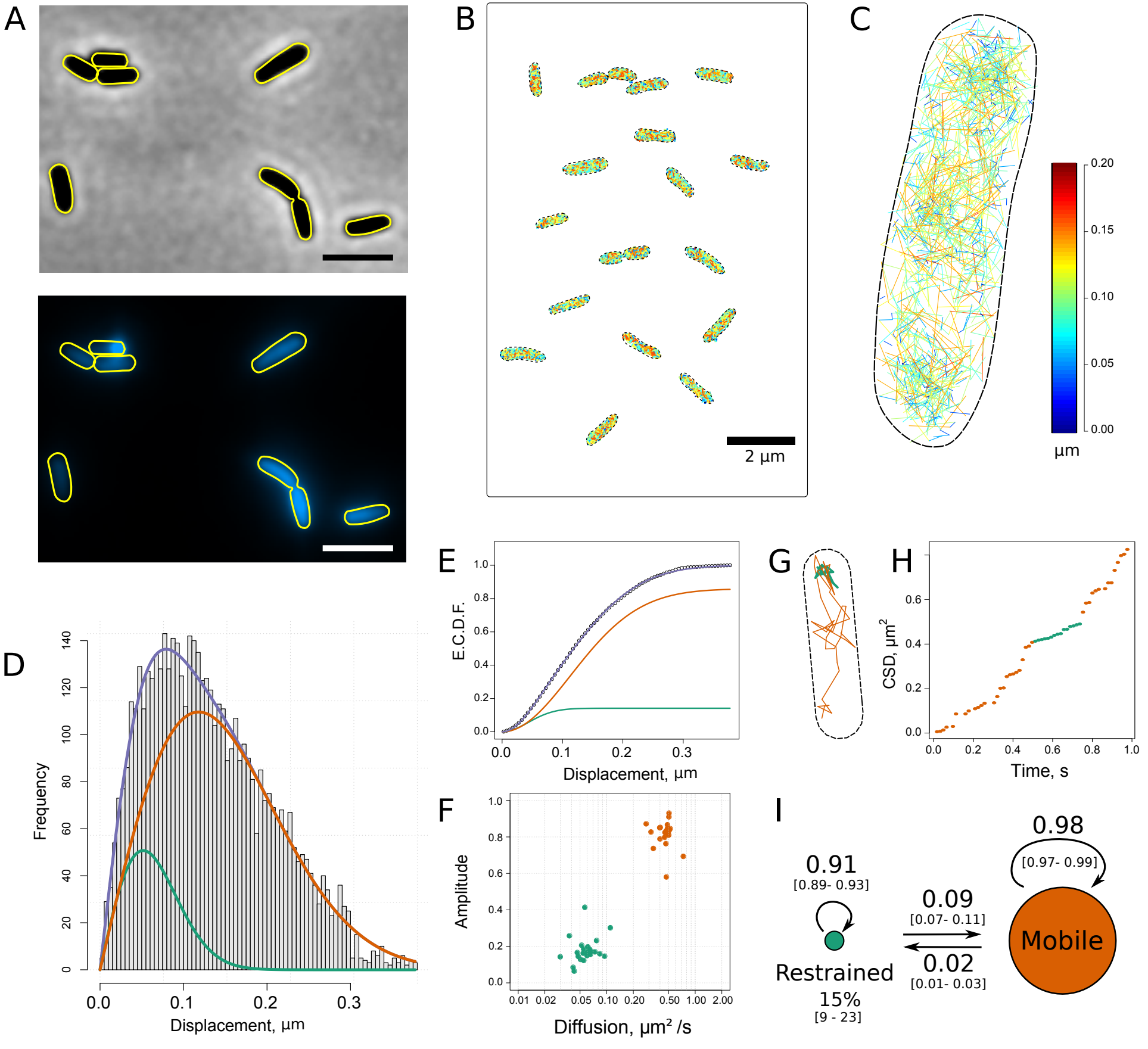
A
B
2 µm
C
0.20
0.15
0.10
0.05
0.00
µm
D
Frequency
Displacement, µm
E
E.C.D.F.
Displacement, µm
F
Amplitude
Diffusion, µm² /s
G
H
CSD, µm²
Time, s
I
0.91
[0.89- 0.93]
Restrained
15%
[9 - 23]
0.09
[0.07- 0.11]
0.02
[0.01- 0.03]
0.98
[0.97- 0.99]
Mobile

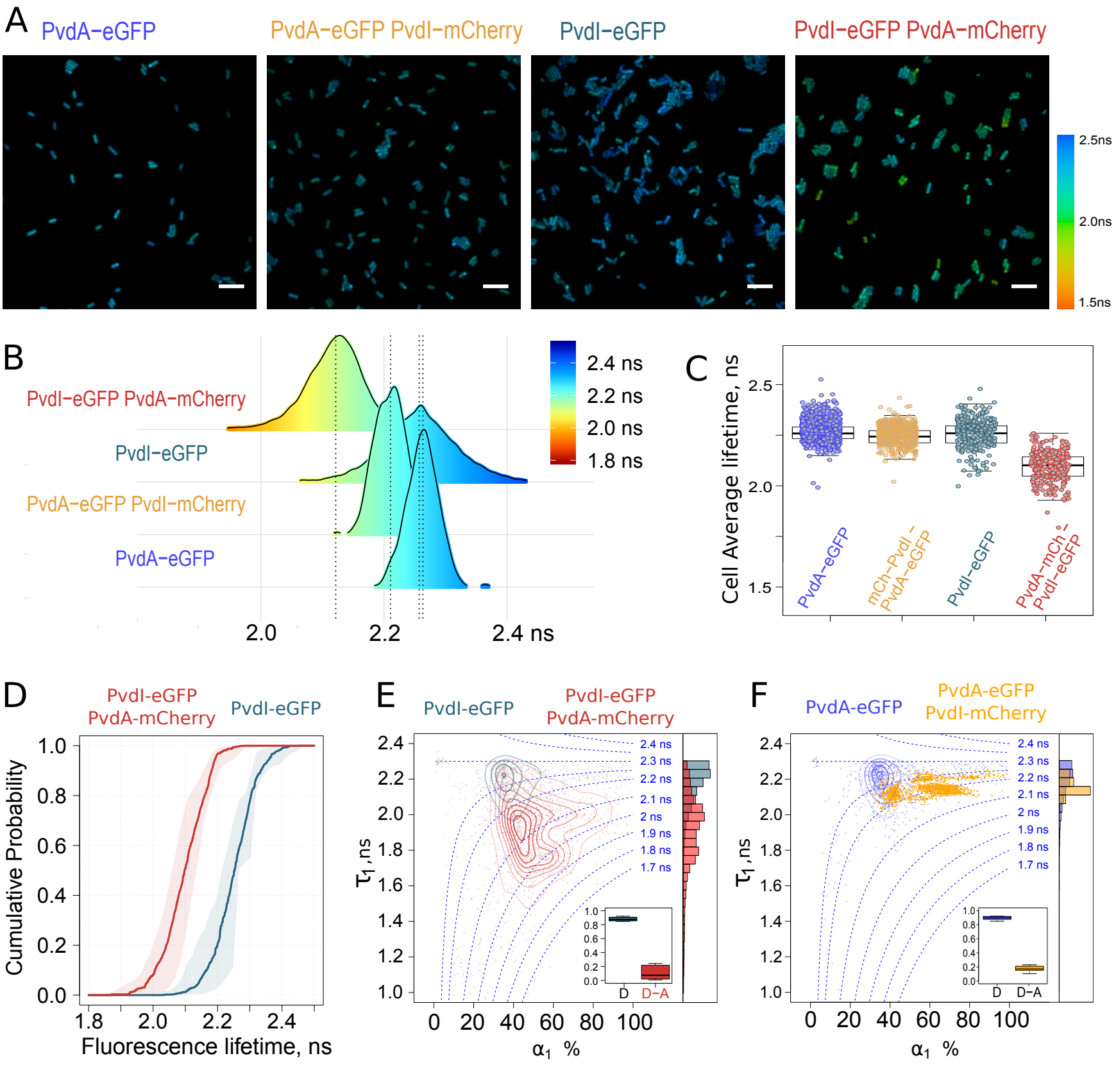
A
PvdA−eGFP
PvdA−eGFP PvdI−mCherry
PvdI−eGFP
PvdI−eGFP PvdA−mCherry
2.5ns
2.0ns
1.5ns
B
PvdI−eGFP PvdA−mCherry
PvdI−eGFP
PvdA−eGFP PvdI−mCherry
PvdA−eGFP
2.4 ns
2.2 ns
2.0 ns
1.8 ns
2.0
2.2
2.4 ns
C
Cell Average lifetime, ns
2.5
2.0
1.5
PvdA−eGFP
mCh−PvdI − PvdA−eGFP
PvdI−eGFP
PvdA−mCh − PvdI−eGFP
D
PvdI-eGFP PvdA-mCherry
PvdI-eGFP
Cumulative Probability
1.0
0.8
0.6
0.4
0.2
0.0
1.8
2.0
2.2
2.4
Fluorescence lifetime, ns
E
PvdI-eGFP
PvdI-eGFP PvdA-mCherry
τ1,ns
2.4
2.2
2.0
1.8
1.6
1.4
1.2
1.0
2.4 ns
2.3 ns
2.2 ns
2.1 ns
2 ns
1.9 ns
1.8 ns
1.7 ns
D
D−A
0
20
40
60
80
100
α1 %
F
PvdA-eGFP
PvdA-eGFP PvdI-mCherry
τ1,ns
2.4 ns
2.3 ns
2.2 ns
2.1 ns
2 ns
1.9 ns
1.8 ns
1.7 ns
D
D−A
α1 %

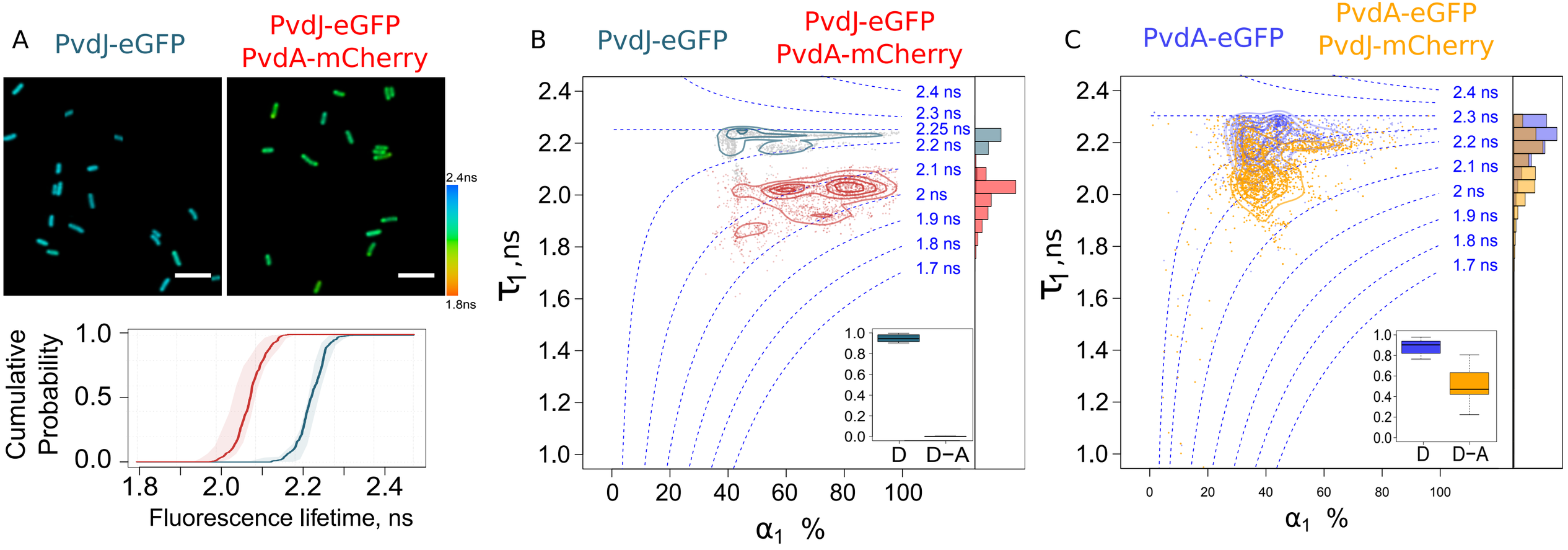
A
PvdJ-eGFP
PvdJ-eGFP
PvdA-mCherry
2.4ns
1.8ns
Cumulative Probability
1.0
0.5
0.0
1.8
2.0
2.2
2.4
Fluorescence lifetime, ns
B
PvdJ-eGFP
PvdJ-eGFP
PvdA-mCherry
2.4 ns
2.3 ns
2.25 ns
2.2 ns
2.1 ns
2 ns
1.9 ns
1.8 ns
1.7 ns
τ1,ns
α1 %
D
D−A
C
PvdA-eGFP
PvdA-eGFP
PvdJ-mCherry
2.4 ns
2.3 ns
2.2 ns
2.1 ns
2 ns
1.9 ns
1.8 ns
1.7 ns
τ1,ns
α1 %
D
D−A

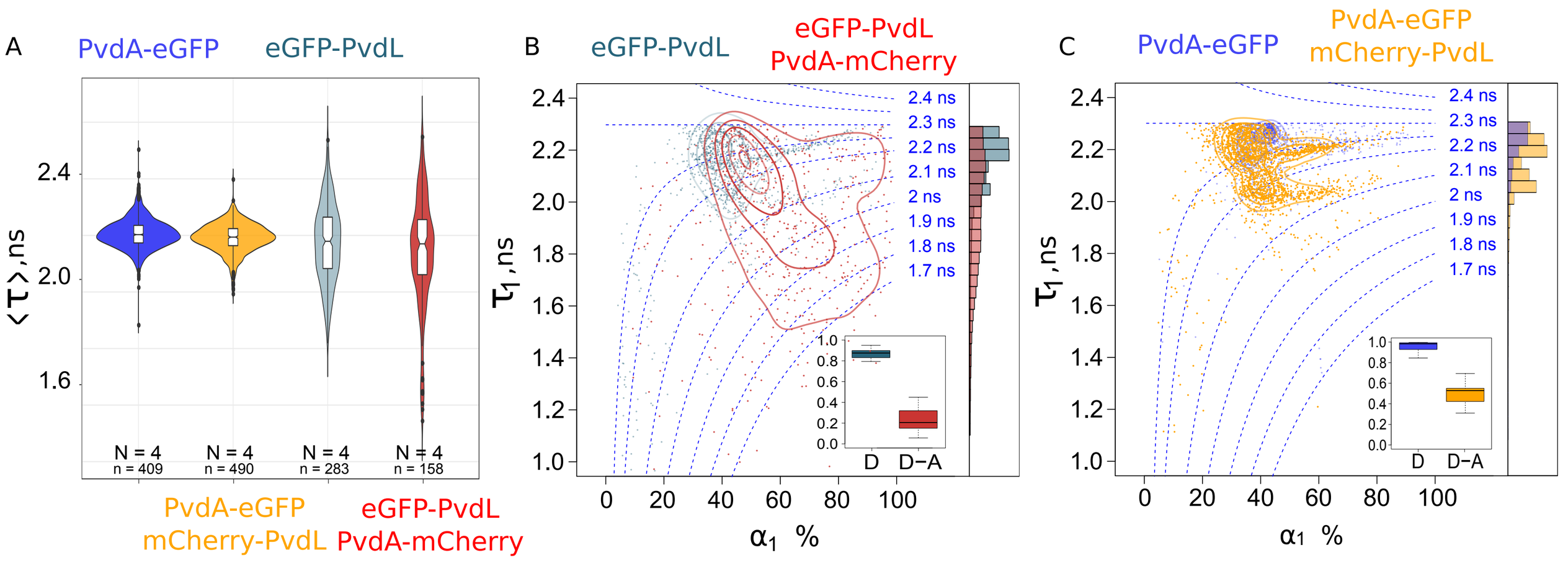
A
PvdA-eGFP
eGFP-PvdL
⟨τ⟩,ns
2.4
2.0
1.6
N = 4
n = 409
N = 4
n = 490
N = 4
n = 283
N = 4
n = 158
PvdA-eGFP
mCherry-PvdL
eGFP-PvdL
PvdA-mCherry
B
eGFP-PvdL
eGFP-PvdL
PvdA-mCherry
τ1,ns
2.4
2.2
2.0
1.8
1.6
1.4
1.2
1.0
2.4 ns
2.3 ns
2.2 ns
2.1 ns
2 ns
1.9 ns
1.8 ns
1.7 ns
1.0
0.8
0.6
0.4
0.2
0.0
D
D−A
0
20
40
60
80
100
α1 %
C
PvdA-eGFP
PvdA-eGFP
mCherry-PvdL
τ1,ns
2.4
2.2
2.0
1.8
1.6
1.4
1.2
1.0
2.4 ns
2.3 ns
2.2 ns
2.1 ns
2 ns
1.9 ns
1.8 ns
1.7 ns
1.0
0.8
0.6
0.4
0.2
0.0
D
D−A
0
20
40
60
80
100
α1 %

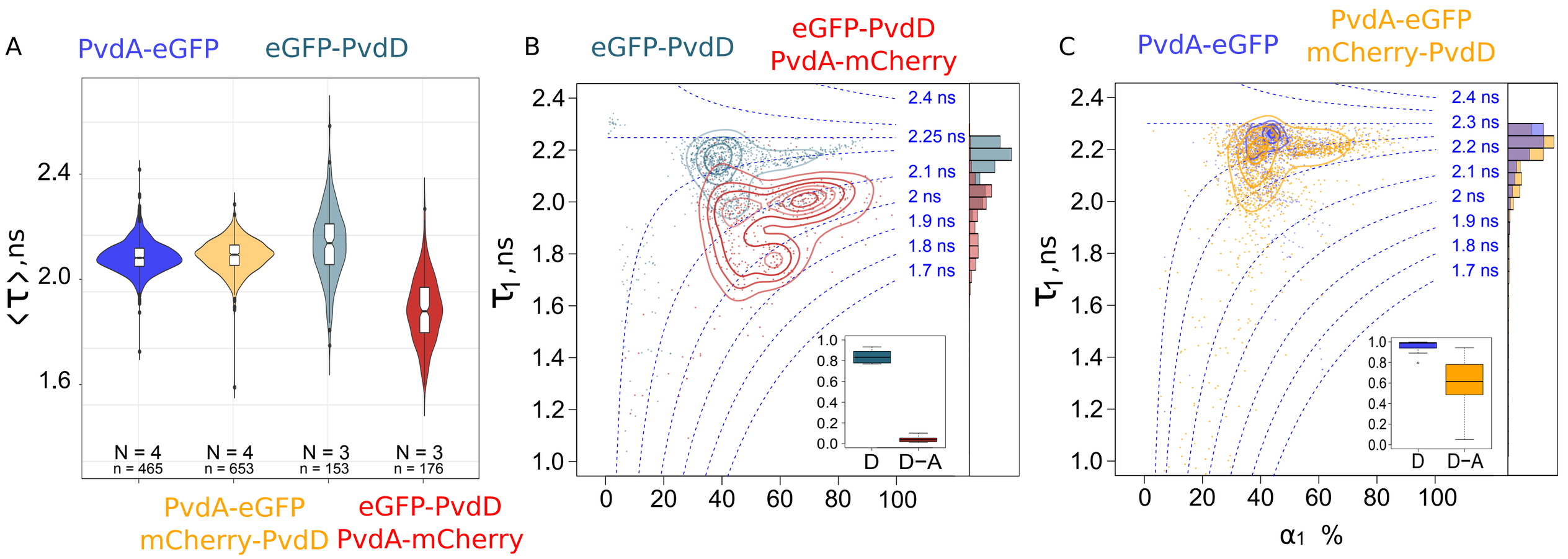
A
PvdA-eGFP
eGFP-PvdD
⟨τ⟩,ns
2.4
2.0
1.6
N = 4
n = 465
N = 4
n = 653
N = 3
n = 153
N = 3
n = 176
PvdA-eGFP
eGFP-PvdD
mCherry-PvdD
PvdA-mCherry
B
eGFP-PvdD
eGFP-PvdD
PvdA-mCherry
τ1,ns
2.4
2.2
2.0
1.8
1.6
1.4
1.2
1.0
2.4 ns
2.25 ns
2.1 ns
2 ns
1.9 ns
1.8 ns
1.7 ns
1.0
0.8
0.6
0.4
0.2
0.0
D
D−A
0
20
40
60
80
100
C
PvdA-eGFP
PvdA-eGFP
mCherry-PvdD
τ1,ns
2.4
2.2
2.0
1.8
1.6
1.4
1.2
1.0
2.4 ns
2.3 ns
2.2 ns
2.1 ns
2 ns
1.9 ns
1.8 ns
1.7 ns
1.0
0.8
0.6
0.4
0.2
0.0
D
D−A
0
20
40
60
80
100
α1 %